



Cite as
Nano-Micro Lett.
(2022) 14:17

Received: 12 July 2021
Accepted: 27 September 2021
© The Author(s) 2021

Carbon-Coated Three-Dimensional MXene/ Iron Selenide Ball with Core–Shell Structure for High-Performance Potassium-Ion Batteries

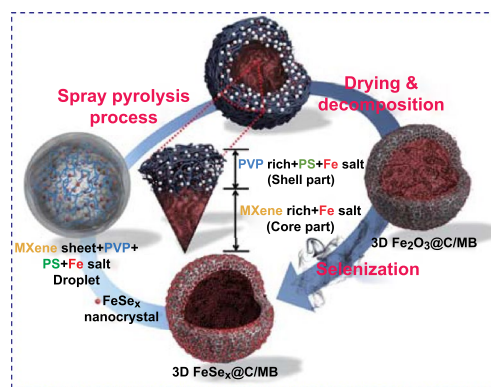
Su Hyun Yang¹, Yun Jae Lee², Heemin Kang¹, Seung-Keun Park² ✉, Yun Chan Kang¹ ✉

HIGHLIGHTS

- We propose a novel synthetic strategy for converting MXene nanosheets into 3D balls coated with iron selenides and carbon (FeSe_x@C/MB), using the ultrasonic spray pyrolysis and thermal treatment.
- Combining iron selenides and carbon with 3D MXene balls offer many more sites for ion storage and enhance the structural robustness of the composite balls.
- The resultant shows high electrochemical performances when used in potassium-ion battery in terms of cycling stability and rate capability.

ABSTRACT Two-dimensional (2D) MXenes are promising as electrode materials for energy storage, owing to their high electronic conductivity and low diffusion barrier. Unfortunately, similar to most 2D materials, MXene nanosheets easily restack during the electrode preparation, which degrades the electrochemical performance of MXene-based materials. A novel synthetic strategy is proposed for converting MXene into restacking-inhibited three-dimensional (3D) balls coated with iron selenides and carbon. This strategy involves the preparation of Fe₂O₃@carbon/MXene microspheres via a facile ultrasonic spray pyrolysis and subsequent selenization process. Such 3D structuring effectively prevents interlayer restacking, increases the surface area, and accelerates ion transport, while maintaining the attractive properties of MXene. Furthermore, combining iron selenides and carbon with 3D MXene balls offers many more sites for ion storage and enhances the structural robustness of the composite balls. The resultant 3D structured microspheres exhibit a high reversible capacity of 410 mAh g⁻¹ after 200 cycles at 0.1 A g⁻¹ in potassium-ion batteries, corresponding to the capacity retention of 97% as calculated based on 100 cycles. Even at a high current density of 5.0 A g⁻¹, the composite exhibits a discharge capacity of 169 mAh g⁻¹.

KEYWORDS MXene; Spray pyrolysis; Iron selenide; Potassium-ion batteries; 3D structures



✉ Seung-Keun Park, skpark09@cau.ac.kr; Yun Chan Kang, yckang@korea.ac.kr

¹ Department of Materials Science and Engineering, Korea University, Anam-Dong, Seongbuk-Gu, Seoul 136-713, Republic of Korea

² Department of Advanced Materials Engineering, Chung-Ang University, 4726 Seodong-daero, Daedeok-myeon, Anseong-si, Gyeonggi-do 17546, Republic of Korea



1 Introduction

K-ion batteries (KIBs) have garnered significant attention for applications in grid energy storage systems, owing to their high energy density and low cost [1–4]. However, developing suitable electrode materials for high-performance KIBs remains challenging because of the sluggish reaction kinetics and huge volume expansion caused by the larger diameter of K^+ than those of Li^+ and Na^+ [5]. Two-dimensional (2D) materials, including layered transition metal compounds, graphene, and phosphorene, have been considered as promising electrode materials for alkali-ion batteries, owing to their large surface-to-volume ratio and short diffusion pathways [6–10].

As a novel family of 2D materials, MXene has been intensively studied as an anode for metal ion batteries in recent years, because of its high metallic conductivity and low diffusion barrier of ions, which lead to fast electron transport and excellent ion diffusion kinetics [11–14]. In addition, theoretical simulations and the corresponding experimental results demonstrated that its electrochemical properties could be further improved by exfoliating multilayer MXene nanosheets into a few layers [15, 16]. Unfortunately, as is the case with most 2D materials, aggregation and restacking between MXene nanosheets easily occurs during the drying and electrode preparation steps, owing to the van der Waals attraction and H-bonding [17]. These drawbacks can decrease the accessibility of ions and the surface area of electrode materials, degrading their electrochemical performance.

Recently, three-dimensional (3D) constructs by self-assembly of MXene nanosheets have been proposed as one of the effective ways to avoid the restacking problem while retaining the unique properties of MXene [18]. This approach not only inhibits the aggregation/restacking between MXene nanosheets, but also enhances the diffusion of ions, improving the electrochemical performance of the associated electrodes. Correspondingly, several research groups have attempted to develop 3D structured MXene-based electrode materials for high-performance energy storage systems. For example, Gogotsi et al. fabricated 3D MXene hollow spheres for Na-ion storage, using a templated method [17]. The obtained hollow spheres had excellent structural stability and exhibited significantly improved Na-ion storage performance, compared with multilayer MXene. Xu et al. proposed a facile approach for directly transforming

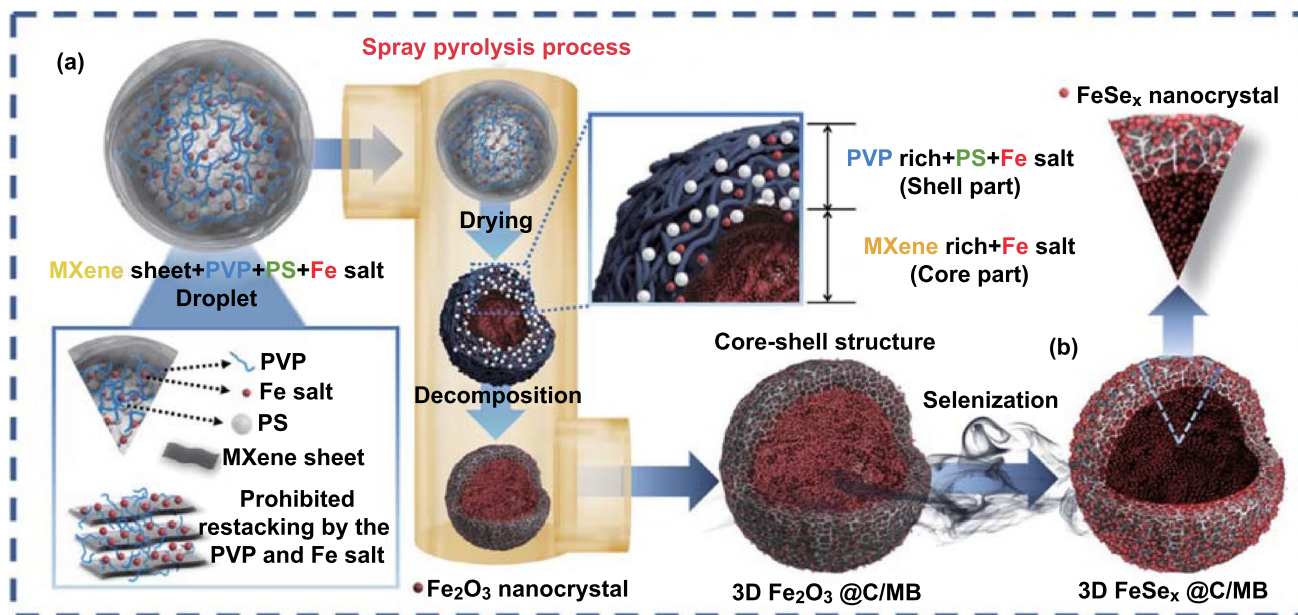
MXene nanosheets into 3D carbon-coated MXene architectures [19]. This was achieved by the self-polymerization of dopamine, and the resulting composites exhibited excellent electrochemical performance for Li/Na-ion batteries. Nevertheless, the intrinsically low specific capacity of MXene hinders its applicability. To overcome this problem, it has been proposed to combine MXene with transition metal chalcogenides (TMCs), of which iron selenide is attracting attention as an anode of batteries due to its high theoretical capacity [20–23]; however, facile production of 3D structured MXene/TMC electrode materials without aggregation remains challenging.

Ultrasonic spray pyrolysis is a scalable and cost-effective technique based on the aerosol process, which has been utilized for synthesizing various structured nanomaterials [24–26]. In particular, this method allows to easily transform low-dimensional materials into 3D spheres by a rapid evaporation of droplets. Nevertheless, synthesis of 3D MXene-based electrode materials for high-performance KIBs using the ultrasonic spray pyrolysis approach has been rarely reported until now.

Herein, we propose a novel synthetic strategy for converting MXene nanosheets into 3D balls coated with iron selenides and carbon, using the ultrasonic spray pyrolysis approach, followed by a thermal treatment (denoted as $FeSe_x@C/MB$). Structuring 2D MXene in 3D could effectively prevent restacking between interlayers, increase surface area, and accelerate ion transport, while maintaining the attractive properties of MXene. Furthermore, combining iron selenides and carbon with 3D MXene balls (denoted as MBs) offers many more sites for ion storage and enhances the structural robustness of the composite balls. The resultant $FeSe_x@C/MB$ anodes exhibit a high reversible capacity, long cycling stability, and excellent rate capability when used in KIBs.

2 Experimental Section

3D MXene balls (MBs) decorated with iron selenides and carbon ($FeSe_x@C/MB$) were synthesized by ultrasonic spray pyrolysis and subsequent thermal treatment for selenization under a reducing atmosphere. MXene sheets were prepared by etching and freeze-drying, as reported previously [27]. Then, the obtained MXene sheets (0.4 g) were dispersed in $Fe(NO_3)_3 \cdot 9H_2O$ (0.02 M, Fe nitrate, 98.5%, SAMCHUN),



Scheme 1 Formation mechanism of $\text{FeSe}_x\text{/C/MB}$ by a facile two-step strategy

polyvinylpyrrolidone (1.0 g, PVP, 40,000, Kanto), polystyrene nanobeads (12 g, PS), in DI water (200 mL), using ultrasonication and stirring. Droplets formed by an ultrasonic humidifier were carried by the N_2 gas into a tubular reactor to produce $\text{Fe}_2\text{O}_3\text{/C/MB}$ (the temperature of the tubular reactor was maintained at $700\text{ }^\circ\text{C}$ with a flow rate of 10 L min^{-1}). The collected $\text{Fe}_2\text{O}_3\text{/C/MB}$ was selenized at $270\text{ }^\circ\text{C}$ under an $\text{H}_2\text{/Ar}$ atmosphere for 12 h at a ramping rate of $2\text{ }^\circ\text{C min}^{-1}$, to form $\text{FeSe}_x\text{/C/MB}$. For comparison, the 3D MBs decorated with only iron selenides ($\text{FeSe}_x\text{/MB}$) were synthesized by the same process as $\text{FeSe}_x\text{/C/MB}$, except for the application of PVP as a carbon source. Bare $\text{FeSe}_2\text{-Fe}_2\text{O}_3$ and 3D MBs were also prepared by the same procedure from spray solutions with iron salt and MXene nanosheets, respectively. The characterization and electrochemical measurements of the synthesized samples are provided in the Electronic Supplementary Material.

3 Results and Discussion

3.1 Synthesis and Characterization of $\text{FeSe}_x\text{/C/MB}$, $\text{FeSe}_x\text{/MB}$, MB, and Bare $\text{FeSe}_2\text{-Fe}_2\text{O}_3$

The formation mechanism of $\text{FeSe}_x\text{/C/MB}$ using a facile two-step strategy is illustrated in Scheme 1. $3\text{D Fe}_2\text{O}_3\text{/C/}$

MB was directly fabricated from a colloidal solution droplet containing MXene nanosheets, polystyrene (PS) nanobeads, polyvinylpyrrolidone (PVP), and Fe nitrate by spray pyrolysis (Scheme 1a). Owing to the small size of the aerosol droplets, rapid evaporation of the solvent occurred upon heating, inducing a strong inward capillary force. This allowed the restructuring of the MXene nanosheets into a 3D structure after complete drying of the solvent. Simultaneously, the phase separation of PVP occurred owing to its low melting point ($\sim 180\text{ }^\circ\text{C}$), which caused most of the PVP to be present in the outer region of the dried microspheres. As the dried microspheres were continuously heated while passing through the reactor, carbonization of PVP and decomposition of PS nanobeads and Fe nitrate occurred, resulting in $3\text{D Fe}_2\text{O}_3\text{/C/MB}$. The MXene balls formed from the high-stiffness nanosheets by spray pyrolysis had plentiful polygonal empty voids. After selenization under a reducing atmosphere, $3\text{D Fe}_2\text{O}_3\text{/C/MB}$ transformed into $\text{FeSe}_x\text{/C/MB}$, in which ultrafine iron selenide nanocrystals were uniformly decorated within the C/MB matrix (Scheme 1b). The formation schemes of $\text{FeSe}_x\text{/MB}$, $\text{FeSe}_2\text{-Fe}_2\text{O}_3$, and MB as comparison samples are shown in Fig. S1. Porous $\text{Fe}_2\text{O}_3\text{/MB}$ and densely structured Fe_2O_3 microspheres formed by spray pyrolysis transformed into $\text{FeSe}_x\text{/MB}$ with grown FeSe_x crystals and $\text{FeSe}_2\text{-Fe}_2\text{O}_3$ composites by selenization,

respectively (Fig. S1a, b). 3D MB microspheres were formed by the one-step spray pyrolysis process from a colloidal solution of MXene nanosheets and PS nanobeads. Restacking of exfoliated 2D MXene nanosheets occurred even within droplets several micrometers in size, as shown in Fig. S1c. However, PVP and Fe-nitrate prevented the restacking of exfoliated 2D MXene nanosheets during the drying stage of the droplets, as described in Scheme 1a.

The overall morphologies of 3D $\text{Fe}_2\text{O}_3@\text{C}/\text{MB}$ and $\text{FeSe}_x@\text{C}/\text{MB}$ are shown in Fig. S2. Regardless of the selenization process, the composite microspheres had a spherical shape with a slightly deflated structure, owing to the shrinkage of the MXene nanosheets during the spray pyrolysis process. Numerous pores were clearly observed on the outer layer of 3D $\text{Fe}_2\text{O}_3@\text{C}/\text{MB}$ (Fig. S2a, b), which could be owing to the thermal decomposition of the PS nanobeads within the MXene-free layer. In addition, the unique core-shell structure of the composites was confirmed by the

distinct contrast between the outer and inner regions, as indicated by the red dashed circle. The X-ray diffraction (XRD) data (Fig. 1a) confirmed the transformation of cubic Fe_2O_3 nanocrystals into iron selenide nanocrystals of hexagonal FeSe and orthorhombic FeSe_2 mixed phases. The characteristic peaks of MXene were not observed in the XRD patterns of 3D $\text{Fe}_2\text{O}_3@\text{C}/\text{MB}$ and $\text{FeSe}_x@\text{C}/\text{MB}$, owing to the presence of FeSe_x nanoparticles decorated on MXene. Instead, from the XRD pattern of MB, it is confirmed that the intrinsic crystal phase of MXene hardly changed during the spray pyrolysis process (Fig. S3). Furthermore, in the inset of Fig. S3, the (002) peak related to the stacking of MXene layers is shifted toward smaller angles, implying an expanded layer of MXene during the spray pyrolysis process [28, 29]. Additionally, to verify the presence of MXene in $\text{FeSe}_x@\text{C}/\text{MB}$, a new sample was prepared by reducing the amounts of the Fe nitrate and PVP to 1/10 while maintaining that of MXene (denoted as $\text{FeSe}_x@\text{C}/\text{MB}-1/10$), and then was analyzed by

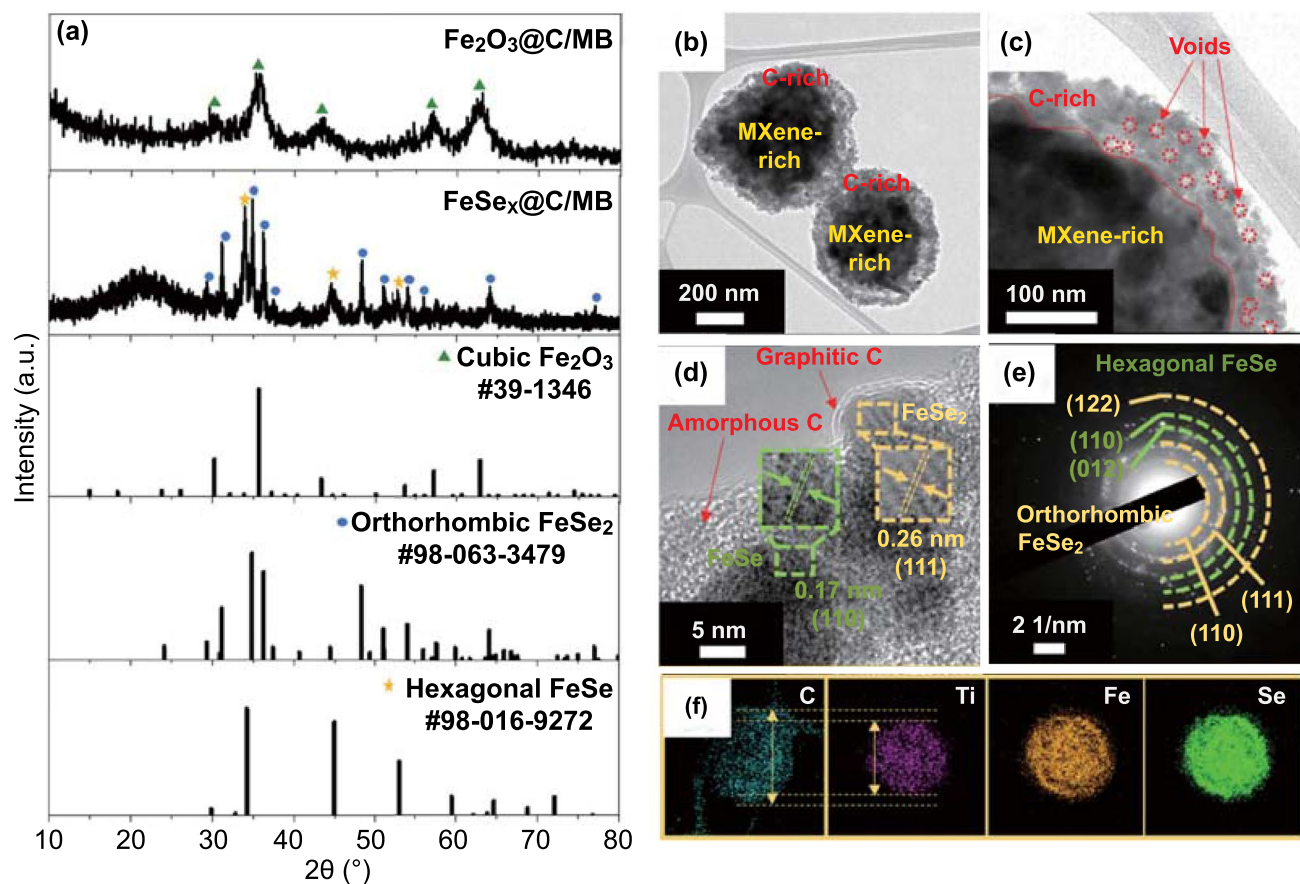


Fig. 1 a XRD patterns of $\text{Fe}_2\text{O}_3@\text{C}/\text{MB}$ and $\text{FeSe}_x@\text{C}/\text{MB}$, b, c TEM images, d HR-TEM image, e SAED pattern, and f elemental mapping images of $\text{FeSe}_x@\text{C}/\text{MB}$

the XRD. As can be seen in Fig. S4a, the surface roughness of FeSe_x@C/MB-1/10 was slightly different from that of the original FeSe_x@C/MB, which was closer to that of 3D MB due to the reduced amounts of Fe nitrate and PVP. In the XRD pattern (Fig. S4b) a distinct peak corresponding to the (002) plane was observed at 8.3°, which is related to the stacking of MXene layers. The broad peak confirmed at 20–25° could be attributed to SiO₂ holder for XRD the measurement. In light of these results, it is considered that the diffraction peaks of MXene were not observed in the XRD pattern of FeSe_x@C/MB due to the relatively large amount of FeSe₂ and its high crystallinity.

The transmission electron microscopy (TEM) image of FeSe_x@C/MB showed a core–shell structure with numerous voids on the outer layer (Fig. 1b). From the magnified TEM image (Fig. 1c), a distinct contrast between the inner and outer regions was confirmed. The measured shell thickness was approximately 70 nm. High-resolution TEM (HR-TEM) images revealed that the FeSe_x nanoparticles were well embedded in the amorphous carbon matrix formed by the carbonization of PVP upon the spray pyrolysis process (Fig. 1d). Interestingly, despite the relatively low synthesis temperature, graphitic layers were identified on the surfaces of some particles, which could be owing to the catalytic effect of metallic Fe nanocrystals formed during the selenization process. In addition, the lattice distances of 0.26 and 0.17 nm were confirmed for the crystalline particles, corresponding to the (111) and (110) planes of FeSe₂ and FeSe crystal phases, respectively. The results of selected area electron diffraction (SAED) data in Fig. 1e reveal that the nanoparticles had a dominant orthorhombic FeSe₂ crystal phase and a minor hexagonal FeSe crystal phase without other impurities. Notably, no patterns related to MXene were identified in the SAED results. Instead, the existence of MXene was clearly confirmed by the elemental mapping images (Fig. 1f). These results show that C, Fe, and Se elements were uniformly distributed over the microspheres, while most Ti elements were only detected in the inner region, indicating that most of the MXene was present inside the microspheres. Furthermore, for accurate comparison, the mapping images of C and Ti element were superimposed as follow (Fig. S5).

X-ray photoelectron spectroscopy (XPS) analysis also revealed the coexistence of C, Ti, Fe, Se, and O elements in 3D FeSe_x@C/MB (Fig. S6). The high-resolution Fe 2p spectrum (Fig. 2a) was resolved into three pairs of

doublets for FeSe₂ (706.3/719.2 eV), FeSe/selenite (2+) (710.0/723.4 eV), and selenite (3+) (712.3/725.7 eV), along with weak peaks from the satellites (714.8 and 717.3 eV/728.2 and 730.7 eV) [30, 31]. The Se 3d spectrum (Fig. 2b) showed three different peaks of Se 3d_{5/2}, Se 3d_{3/2}, and selenite. The first two peaks were attributed to iron selenides, and the other one was owing to the partial oxidation of 3D FeSe_x@C/MB [32, 33]. The Ti 2p spectrum (Fig. 2c) showed multiple component peaks corresponding to Ti–C, Ti³⁺, Ti⁴⁺, and C–Ti–F bonds, indicating that the MXene nanosheets with the chemical formula of Ti_{n+1}C_nF_x were partially oxidized during the spray pyrolysis process [34–37]. The C 1s (Fig. 2d) spectrum could be deconvoluted into five peaks for Ti–C (282.5 eV), C=C (284.0 eV), C–C (285.2 eV), C–O (286.1 eV), and O=C–O (288.1 eV) bonds. The presence of the Ti–C bond was ascribed to MXene [37, 38].

In the case of 3D Fe₂O₃/MB prepared without adding PVP, no outer pores or core–shell structures were identified, indicating that PVP plays an important role in controlling the structure of the composites (Fig. S7a, b). After selenization under a reducing atmosphere, the Fe₂O₃ nanoparticles were transformed into FeSe_x nanoparticles, forming 3D FeSe_x/MB. The morphology of 3D FeSe_x/MB was similar to that of 3D FeSe_x@C/MB. However, unlike 3D FeSe_x@C/MB, 3D FeSe_x/MB consisted of rod-shaped nanoparticles that were the result of the overgrowth of FeSe_x owing to the Ostwald ripening (Fig. S7c, d) [39]. Although 3D Fe₂O₃@C/MB and Fe₂O₃/MB had different structural features, the XRD patterns of Fe₂O₃/MB corresponded to the crystal phases of cubic Fe₂O₃, and Fe₂O₃ nanocrystals transformed into iron selenide nanocrystals of hexagonal FeSe and orthorhombic FeSe₂ mixed phases after selenization (Fig. 3a).

As shown in Fig. 3b, the FeSe_x nanorods had irregular sizes and morphologies, and mostly exposed on the surface of the 3D MXene balls. In light of these results, the carbon matrix in 3D FeSe_x@C/MB effectively inhibited the overgrowth of FeSe_x during the selenization process. TEM image (Fig. 3c) showed clear empty voids owing to the stiffness of the MXene nanosheets and PS nanobeads. HR-TEM imaging (Fig. 3d) confirmed the lattice fringes with distances of 0.29, 0.26, and 0.43 nm, which were indexed to the (101), (011), and (006) planes of FeSe₂, FeSe, and MXene, respectively. The XRD and SAED patterns of 3D FeSe_x/MB were similar to those of 3D FeSe_x@C/MB (Fig. 3a, e). The mapping images of C, Ti, Fe, and Se overlapped well with each other (Fig. 3f).

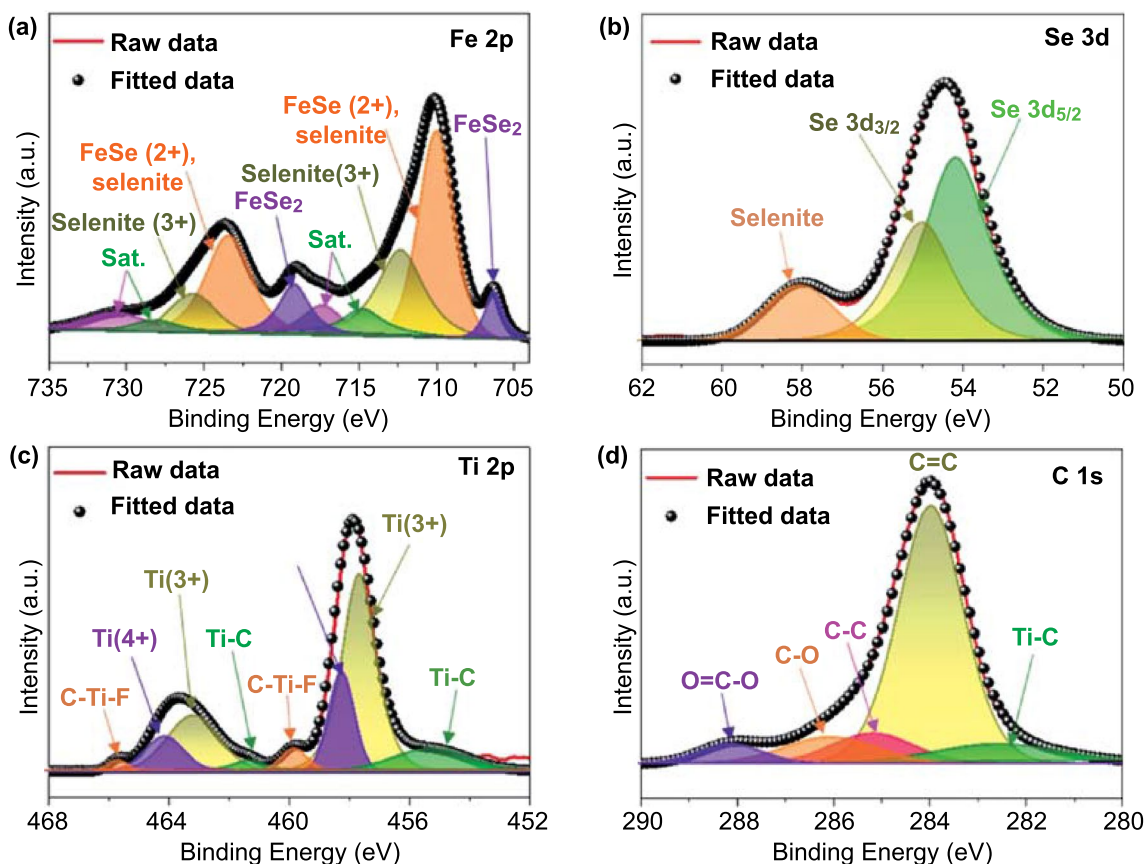


Fig. 2 XPS spectra of $\text{FeSe}_x\text{/C/MB}$: **a** Fe 2p, **b** Se 3d, **c** Ti 2p, and **d** C 1s spectra

A 3D MXene ball with numerous surface ridges was also synthesized as a comparison sample by spray pyrolysis of a spray solution containing only MXene nanosheets (Fig. S8). The MXene ball reported previously exhibited a typical 2D layer with a lateral size of several tens of micrometers. On the other hand, similar structured reduced graphene oxide balls did not show a clear 2D layer. The stiffness of the 2D MXene nanosheets (Fig. S8a, b) resulted in a uniquely structured 3D ball with plentiful polygonal empty voids (Fig. S8c, d). HR-TEM imaging confirmed a few layers separated by 1.26 and 0.15 nm, corresponding to the (002) and (110) planes of the MXene nanosheets (Fig. S8e). Elemental mapping images (Fig. S8f) exhibited an even distribution of C, Ti, and O throughout the 3D MXene ball.

The synthesis of bare FeSe_x microspheres as a comparison sample was also attempted by selenization of Fe_2O_3 microspheres, which were synthesized by spray pyrolysis from a spray solution with only Fe nitrate. The scanning electron microscopy (SEM) images (Fig. S9a, b) show that the

surfaces of the polydisperse microspheres became rougher than before selenization. However, $\text{FeSe}_2\text{-Fe}_2\text{O}_3$ composite microspheres were formed by the incomplete selenization of dense Fe_2O_3 microspheres. As can be seen in the XRD patterns (Fig. S9c), the microspheres exhibited a typical Fe_2O_3 crystalline phase before the selenization, but after the selenization, two different crystal phases (orthorhombic FeSe_2 and hexagonal Fe_2O_3) were observed. The incomplete phase transformation into the metal selenide could be owing to the dense structure of the $\text{FeSe}_2\text{-Fe}_2\text{O}_3$ microspheres, which precluded the H_2Se gas from penetrating into the microspheres.

The N_2 adsorption–desorption isotherm results revealed that the 3D MXene ball had a higher specific surface area ($64.8 \text{ m}^2 \text{ g}^{-1}$) relative to pristine 2D MXene ($7.6 \text{ m}^2 \text{ g}^{-1}$), proving that 3D structuring can effectively inhibit the restacking of MXene (Fig. S10a). In addition, compared with the 3D MXene ball, the slightly reduced specific surface areas of 3D $\text{FeSe}_x\text{/MB}$ ($52.9 \text{ m}^2 \text{ g}^{-1}$) and $\text{FeSe}_x\text{/C/MB}$

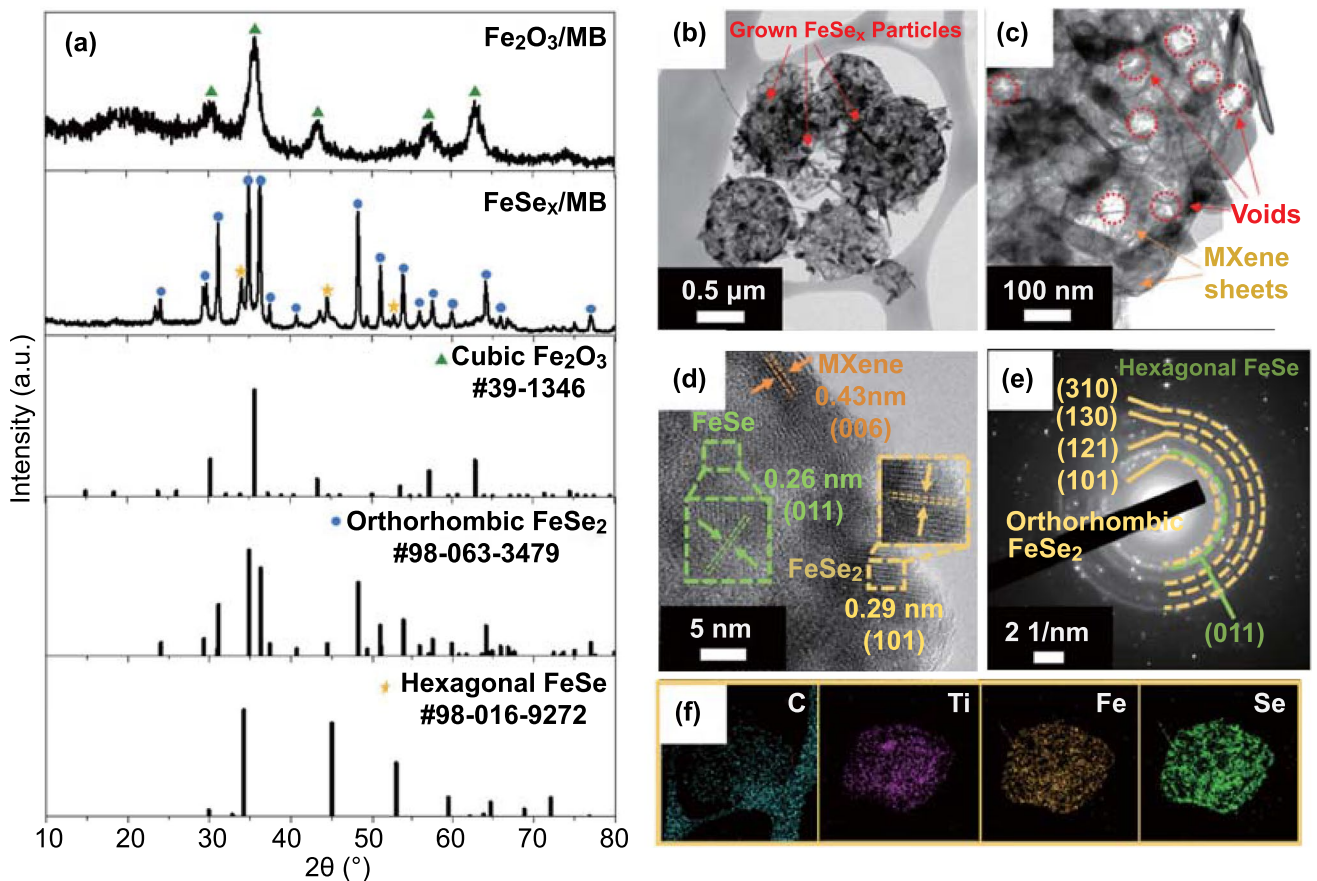


Fig. 3 a XRD patterns of $\text{Fe}_2\text{O}_3/\text{MB}$ and FeSe_x/MB , b, c TEM images, d HR-TEM image, e SAED pattern, and f elemental mapping images of FeSe_x/MB

($22.7 \text{ m}^2 \text{ g}^{-1}$) could be ascribed to the presence of FeSe_x crystals and carbon matrix (Fig. S10b). Meanwhile, the $\text{FeSe}_2\text{-Fe}_2\text{O}_3$ microspheres exhibited an extremely small specific surface area ($0.2 \text{ m}^2 \text{ g}^{-1}$), owing to their dense structure. From the Barrett–Joyner–Halenda (BJH) pore-size distribution data (Fig. S10c, d), 3D MXene-based materials

were confirmed to have well-developed meso- and macroporous structures, consistent with the SEM and TEM results.

Figure 4 displays the Raman spectra of the 3D FeSe_x/MB and $\text{FeSe}_x@\text{C}/\text{MB}$ composites and TG curves of $\text{FeSe}_x@\text{C}/\text{MB}$, FeSe_x/MB , and MB. In Fig. 4a, the 3D FeSe_x/MB and $\text{FeSe}_x@\text{C}/\text{MB}$ samples exhibited three peaks (178.1, 214.4,

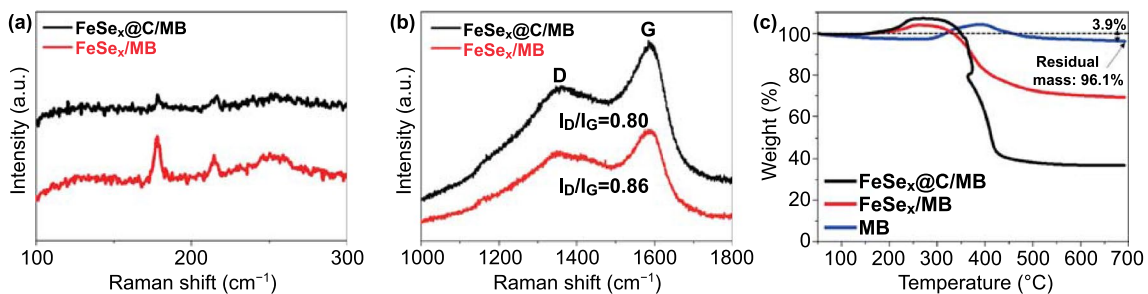


Fig. 4 a, b Raman spectra of $\text{FeSe}_x@\text{C}/\text{MB}$ and FeSe_x/MB and c TG curves of $\text{FeSe}_x@\text{C}/\text{MB}$, FeSe_x/MB , and MB

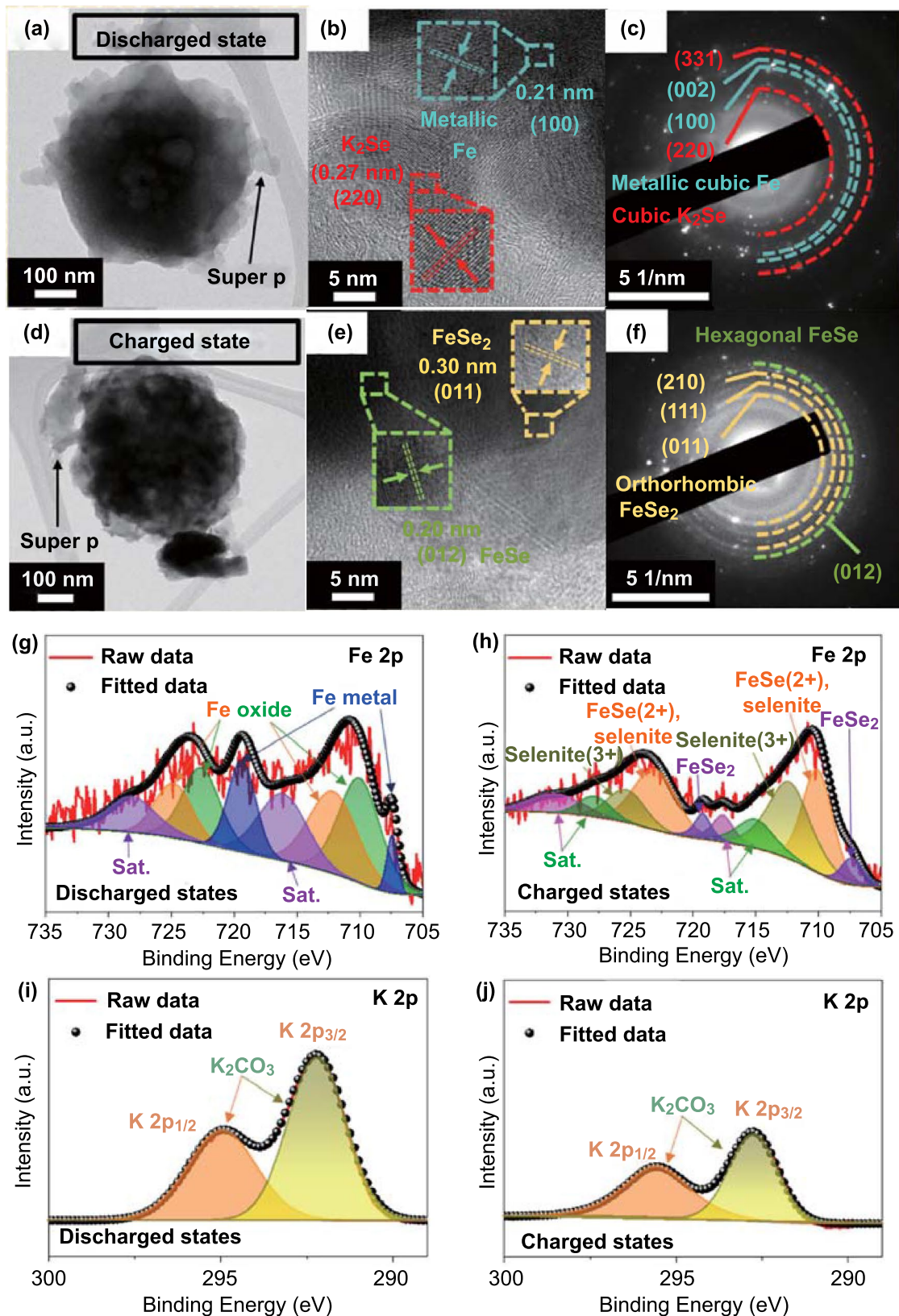


Fig. 5 *Ex-situ* TEM images, SAED patterns, XPS spectra of FeSe_x@C/MB after the first discharge (a–c, g, i) and charge state (d–f, h, j): a, d TEM images, b, e HR-TEM images, c, f SAED patterns, g, h Fe 2p, and i, j K 2p spectra

and 250.2 cm^{-1}) in the $100\text{--}300\text{ cm}^{-1}$ region. Based on previous reports, the peak at 214.4 cm^{-1} was a Se-Se stretching mode, and the peaks at 178.1 and 250.2 cm^{-1} were Se-Se librational and stretching vibrations or their combination of Fe-Se bonds, respectively [40, 41]. In addition, the D and G bands in the $1200\text{--}1800\text{ cm}^{-1}$ region indicate the presence of amorphous carbon with numerous defects in the composites (Fig. 4b) [42, 43]. Interestingly, even though no carbon source was added, the D and G bands were identified in the FeSe_x/MB sample, which could be owing to the reordering of C atoms lost in MXene during the annealing, as reported in previous studies [44].

In the thermal gravimetric analysis (TGA) results (Fig. 4c), the 3D MB sample showed an initial weight increase for temperatures in the $300\text{--}400\text{ }^\circ\text{C}$ range, followed by a weight loss, which could be attributed to the oxidation of MXene into TiO_2 and to the release of the CO_2 gas [45]. The final weight loss of the 3D MB sample was 3.9%. Meanwhile, the TGA curves of FeSe_x/MB and $\text{FeSe}_x@C/\text{MB}$ showed a similar initial weight increase for temperatures in the $250\text{--}300\text{ }^\circ\text{C}$ range, corresponding to a partial oxidation of metal selenides to metal selenates and SeO_2 [46]. The subsequent weight loss could be attributed to the combustion of carbonaceous material and further oxidation of metal selenides to metal oxides. Due to the presence of PVP derived carbon, $\text{FeSe}_x@C/\text{MB}$ exhibited greater weight loss for temperatures in the $300\text{--}400\text{ }^\circ\text{C}$. Based on these results, the carbon content of the 3D $\text{FeSe}_x@C/\text{MB}$ composite was determined to be 32.5%.

3.2 Investigation of K-Ion Storage Mechanism and KIB Performances

To confirm the electrochemical conversion mechanism of $\text{FeSe}_x@C/\text{MB}$ during potassiation/depotassiation, *ex-situ* TEM and XPS analyses were conducted at the first discharged and charged states (Fig. 5). In the *ex-situ* TEM images (Fig. 5a, d), the overall morphology of the composite was well maintained, but the detailed structure could not be verified owing to the presence of a polymeric layer formed after the cycling. After the fully discharged state, HR-TEM imaging (Fig. 5b) revealed the crystal lattice fringes separated by 0.21 and 0.27 nm, which were indexed to the (100) plane of metal cubic Fe and to the (220) plane of cubic K_2Se , respectively. The relevant rings in the SAED pattern (Fig. 5c) also matched well the metal cubic Fe and

K_2Se . These results suggest that iron selenides in $\text{FeSe}_x@C/\text{MB}$ are converted into metal Fe nanoparticles after full discharge. At that time, the K_2Se by-product was also formed through the reaction between potassium and Se ions. In the *ex-situ* XRD results of the MB electrode measured after the initial discharge, the (002) peak related to the stacking of MXene layers was barely verified, indicating the expansion of the MXene layer owing to the intercalation of K^+ (Fig. S11) [47]. Meanwhile, the HR-TEM image of $\text{FeSe}_x@C/\text{MB}$ in the fully charged state showed the existence of orthorhombic FeSe_2 and hexagonal FeSe (Fig. 5e). Furthermore, the (002) peak was still not confirmed in the *ex-situ* XRD data after the initial charge. This result suggests that the expanded layers of MXene remained after the extraction of K^+ ions [47], and metal Fe nanoparticles returned to the corresponding iron selenides after the charge process. The corresponding SAED pattern rings (Fig. 5f) also show the formation of FeSe_x crystals in a reversible conversion reaction.

In the XPS results, the high-resolution Fe 2p spectrum of $\text{FeSe}_x@C/\text{MB}$ in the fully discharged state shows paired deconvoluted peaks corresponding to Fe metal nanoparticles as well as iron oxide (Fig. 5g). The presence of the oxidized state can be attributed to the properties of metallic particles that are prone to oxidation. Notably, these peaks disappeared after full charging (Fig. 5h), and new peaks appeared with weakened crystallinity. In the K 2p spectrum, the intensity of the peak corresponding to K_2CO_3 was higher in the fully discharged state than in the fully charged state, which could be ascribed to the solid electrolyte interphase (SEI) layer, composed of K_2CO_3 , that became partially decomposed after the charging process (Fig. 5i, j) [48, 49]. These electrochemical conversions also confirm the above-mentioned *ex-situ* TEM results.

The electrochemical impedance spectroscopy (EIS) analysis was carried out *in-situ* during the initial cycle, at a scan rate of 0.05 A g^{-1} , to support the electrochemical conversion mechanism of $\text{FeSe}_x@C/\text{MB}$. In Fig. 6a, the data points indicate the preselected potentials for *in-situ* EIS measurements during potassiation/depotassiation at 0.05 A g^{-1} . The Nyquist plots fitted by the Randle-type equivalent circuit (Fig. S12) and the change in R_{tot} (sum of interfacial resistances related to the SEI (R_{sei}) and to the charge transfer resistance (R_{ct})) are shown in Fig. 6b and c. During the first discharge process, R_{tot} continuously decreased from the potential to -0.05 V , owing to ultrafine metal Fe nanoparticles with high electrical conductivity, as confirmed by the

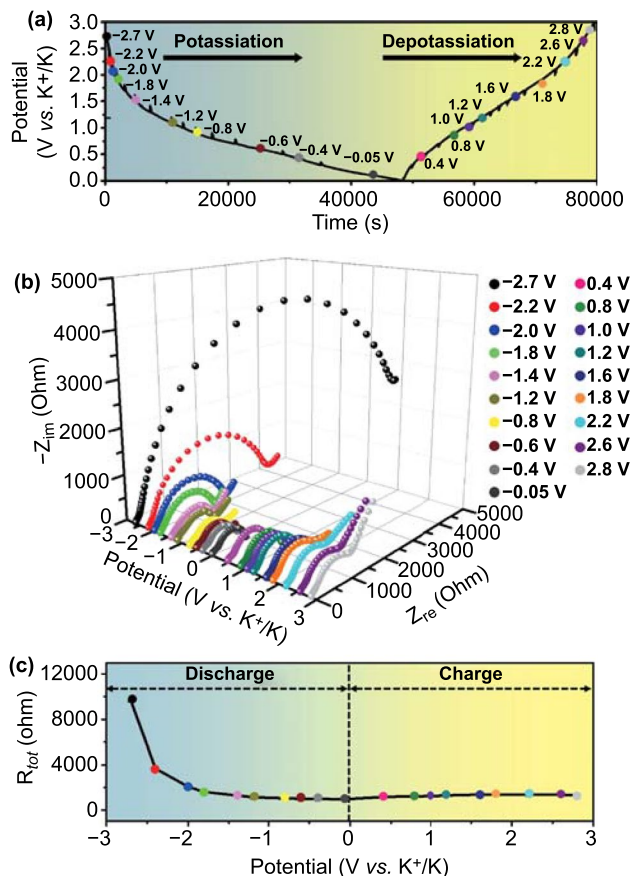


Fig. 6 *In-situ* EIS of $\text{FeSe}_x\text{/C/MB}$: **a** Potential vs. times curve, **b** *in-situ* Nyquist plots, and **c** R_{tot} values obtained at pre-selected potentials during the first cycles at 0.05 A g^{-1}

ex-situ TEM analysis (Fig. 5). During the subsequent charging process, R_{tot} gradually increased until 1.8 V, owing to the structural stress and the phase transformation into FeSe_x , which has a lower electrical conductivity than metallic Fe. Beyond 1.8 V, the reduction of R_{tot} could be owing to the volume contraction induced complete depotassiation and partial decomposition of the SEI layer [50], as confirmed by the *ex-situ* XPS (Fig. 5i, j).

Cyclic voltammetry (CV) was conducted at a scan rate of 0.1 mV s^{-1} , for potentials in the 0.001–3.0 V range (vs. K^+/K) for the first, second, and fifth cycles, to investigate the electrochemical conversion characteristics of the $\text{FeSe}_x\text{/C/MB}$, $\text{FeSe}_x\text{/MB}$, $\text{FeSe}_2\text{-Fe}_2\text{O}_3$, and MB electrodes (Fig. 7a–d). In the first cathodic sweep, $\text{FeSe}_x\text{/C/MB}$ exhibited broad three peaks, in which the peak observed at 2.27 V was associated with the intercalation of K^+ into MB [15], and peaks at 1.18 and 0.45 V corresponded to the

intercalation of K^+ into FeSe_x and the formation of metal Fe and K_2Se from K_xFeSe_y , respectively [51, 52]. In addition, during the subsequent cathodic sweeps, the initial peaks disappeared, and new peaks appeared at a higher potential with low intensity. These peaks imply the irreversible formation of an SEI layer during the first discharge process [53]. In the case of the first anodic sweep, broad peaks were observed at 0.50, 1.05, 1.67, and 2.32 V for $\text{FeSe}_x\text{/C/MB}$. The peak at 0.50 V was related to the extraction of K^+ from MB [15], and the peaks at 1.05, 1.67, and 2.32 V were attributed to the transformation of metallic Fe nanoparticles and K_2Se into FeSe_x nanocrystals [54, 55]. The CV data of $\text{FeSe}_x\text{/MB}$ showed similar tendencies to those of $\text{FeSe}_x\text{/C/MB}$, but the peaks were more apparent than in the case of $\text{FeSe}_x\text{/C/MB}$, owing to the formation of larger FeSe_x crystals in the absence of carbon. On the other hand, CV-shaped $\text{FeSe}_2\text{-Fe}_2\text{O}_3$ microspheres exhibited slightly different trends from those of $\text{FeSe}_x\text{/C/MB}$ and $\text{FeSe}_x\text{/C}$, featuring a peak at 0.66 V, which corresponded to the conversion reaction of Fe_2O_3 [56, 57]. In addition, the area of the CV curve for the $\text{FeSe}_2\text{-Fe}_2\text{O}_3$ microspheres was smaller than those for $\text{FeSe}_x\text{/C/MB}$ and $\text{FeSe}_x\text{/MB}$, implying a lower specific capacity of the $\text{FeSe}_2\text{-Fe}_2\text{O}_3$ microspheres. Meanwhile, MBs exhibited two cathodic peaks at 2.40 and 0.41 V for the first cathodic sweep, which corresponded to the K^+ intercalation reaction and to the formation of the SEI layer, respectively [15, 58]. According to a previous study [17, 59], a high potential is related to an irreversible reaction between the surface functional groups of MXene and the electrolyte, while low-potential peaks are related to the K^+ intercalation in the small interlayer space with the formation of the SEI layer. Moreover, the cathodic peak located in the range of low potentials persisted even after the first sweep, indicating the reversible intercalation and stability of the MXene phase after repeated potassiation/depotassiation.

To probe the K-ion storage performance of $\text{FeSe}_x\text{/C/MB}$, $\text{FeSe}_x\text{/MB}$, $\text{FeSe}_2\text{-Fe}_2\text{O}_3$, and MB electrodes, a galvanostatic charge–discharge test was conducted (Fig. 8). The initial charge–discharge profiles for the four electrodes were obtained at a current density of 0.1 A g^{-1} , and are shown in Fig. 8a. Distinct plateaus were confirmed in the 1.18–1.30 V range for the initial discharge curves of $\text{FeSe}_x\text{/C/MB}$, $\text{FeSe}_x\text{/MB}$, and $\text{FeSe}_2\text{-Fe}_2\text{O}_3$ electrodes. In the case of MB, a plateau corresponding to the intercalation reaction between MXene and K^+ was observed for lower potentials (0.40–0.50 V), in agreement with the CV results. The initial

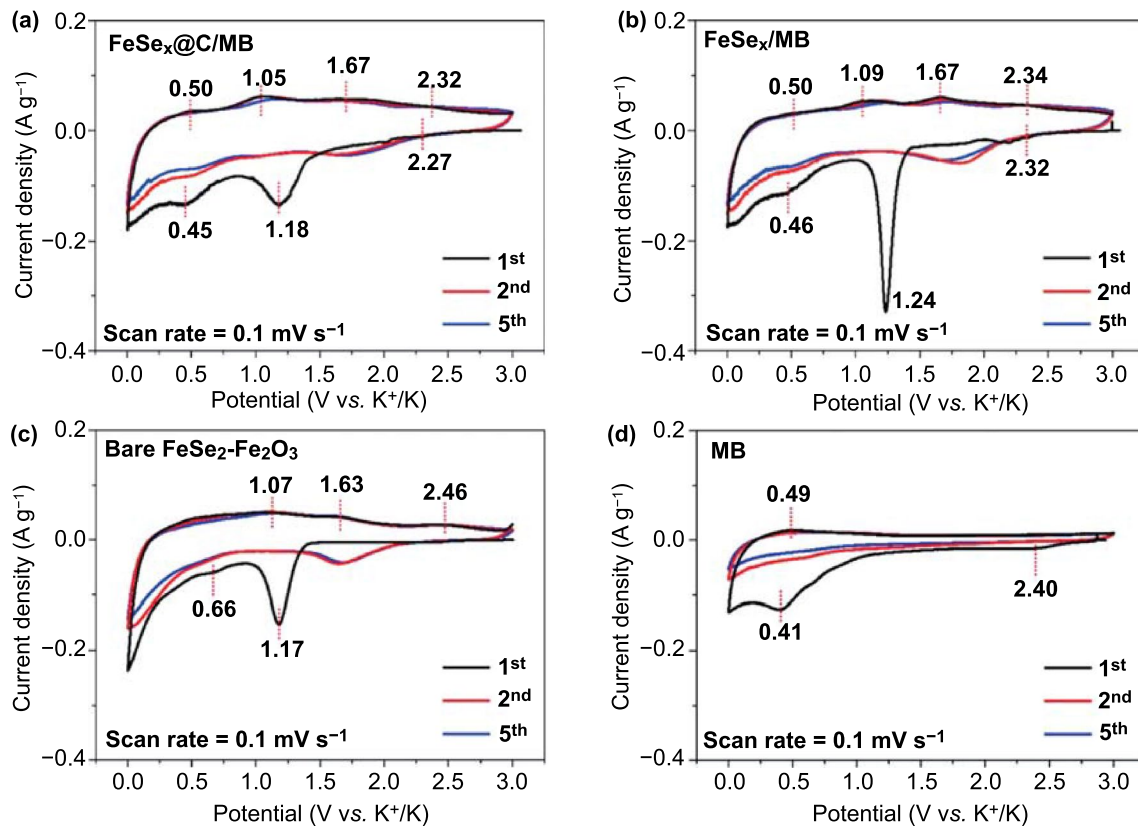


Fig. 7 CV data at voltage range 0.001–3.0 V: **a** FeSe_x@C/MB, **b** FeSe_x/MB, **c** bare FeSe₂-Fe₂O₃, and **d** MB

discharge/charge capacities of the FeSe_x@C/MB, FeSe_x/MB, FeSe₂-Fe₂O₃, and MB electrodes were 579/350, 574/356, 441/304, and 376/109 mAh g⁻¹, and their Coulombic efficiencies (CEs) were 60%, 62%, 69%, and 29%, respectively. Compared with FeSe_x/MB, the lower initial CE of FeSe_x@C/MB could be attributed to the presence of disordered carbon material with a high initial irreversible capacity [60, 61]. Meanwhile, the lowest initial CE of MB was attributed to its high specific surface area, which provided more sites for the formation of an irreversible SEI layer.

Figure 8b shows the cycling performance of the four electrodes, assessed at a current density of 0.1 A g⁻¹. The discharge capacities of the FeSe_x@C/MB, FeSe_x/MB, FeSe₂-Fe₂O₃, and MB electrodes after 200 cycles were 410, 89, 89, and 76 mAh g⁻¹, respectively. The capacity of the FeSe_x@C/MB electrode gradually increased during the first 50 cycles owing to the electrode activation, but then settled at a certain level and remained so without significant degradation until 200 cycles. Moreover, the CEs of FeSe_x@C/MB quickly reached 99% within 10 cycles, and remained at that level during the entire cycle process. On

the other hand, FeSe_x/MB exhibited a rapid capacity decay after 50 cycles and eventually attained capacity similar to that of FeSe₂-Fe₂O₃. Nevertheless, the SEM images of the two electrodes after 200 cycles revealed that the original spherical morphologies of the FeSe_x@C/MB and FeSe_x/MB composites were well retained, without severe structural collapse (Fig. S13a, b). These results indicate that the exposed FeSe_x nanoparticles without carbon coating were easily pulverized during cycling, while the overall morphology of the composites did not collapse owing to the presence of MXene. In previous studies [27, 62], it was noted that this pulverization can occur owing to the different volume expansion rates of active materials and MXene and the weak interaction between them. Meanwhile, the bare FeSe₂-Fe₂O₃ microspheres exhibited a relatively low reversible capacity during the early cycles, owing to the presence of Fe₂O₃ crystals with poor K-ion storage performance, and their capacity decreased faster than that of FeSe_x/MB after the 50th cycle. The SEM image of the bare FeSe₂-Fe₂O₃ electrode after 200 cycles shows the pulverized microspheres, indicating that MB could contribute to the structural stability (Fig. S13c).

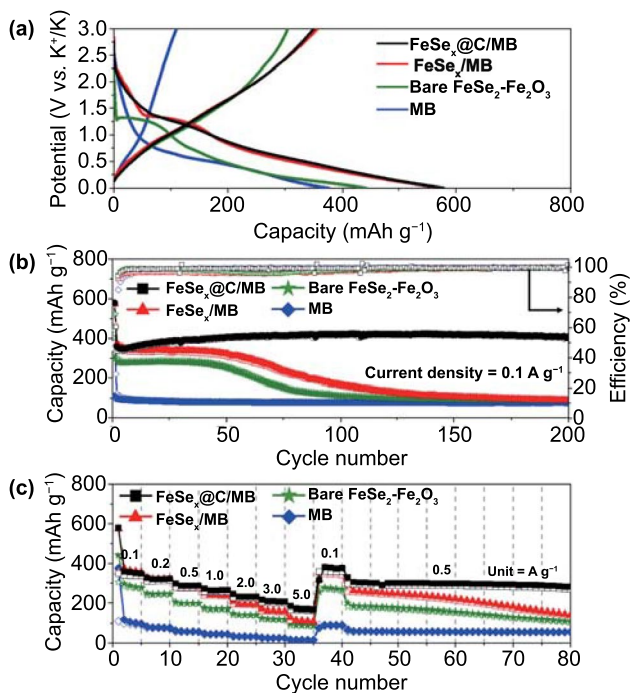


Fig. 8 Electrochemical properties of $\text{FeSe}_x@C/MB$, FeSe_x/MB , bare $\text{FeSe}_2\text{-Fe}_2\text{O}_3$, and MB: **a** initial charge–discharge curves, **b** cycle performances at a current density 0.1 A g^{-1} , and **c** rate performances at various current densities

MB exhibited a low specific capacity but excellent cycling stability, for the entire number of cycles.

The rate performances of the four electrodes were evaluated for various current ranges, from 0.1 to 5.0 A g^{-1} (Fig. 8c). $\text{FeSe}_x@C/MB$ exhibited a stable reversible capacity over the entire range of current densities and yielded discharge capacities of $349, 322, 287, 263, 230, 206,$ and 169 mA g^{-1} at the current densities of $0.1, 0.2, 0.5, 1.0, 2.0, 3.0,$ and 5.0 A g^{-1} , respectively. In addition, when the current density decreased to 0.1 from 5.0 A g^{-1} , the capacity of the $\text{FeSe}_x@C/MB$ electrode mostly recovered, indicating that the structural degradation was minimal at high current densities, owing to the electrode's excellent structural robustness. Furthermore, although the current density increased again to 0.5 A g^{-1} , the electrode's capacity remained high and stable, without any rapid capacity decay. By contrast, FeSe_x/MB exhibited reversible discharge capacities of $357, 323, 277, 237, 191, 158,$ and 109 mA g^{-1} at the current densities of $0.1, 0.2, 0.5, 1.0, 2.0, 3.0,$ and 5.0 A g^{-1} , respectively. Although the FeSe_x/MB electrode exhibited reversible capacities similar to those of the $\text{FeSe}_x@C/MB$ electrode at low current densities, its capacity

decreased more significantly with increasing current density (compared with the $\text{FeSe}_x@C/MB$ electrode). Moreover, the capacity continued to decrease, even at low current densities. In light of these results, we concluded that the carbon layer effectively inhibits the volume expansion of FeSe_x nanoparticles and facilitates electron transport. Compared with previously reported Fe-based anodes for KIBs, the $\text{FeSe}_x@C/MB$ electrode demonstrated superior electrochemical performance, especially in terms of cycling stability and specific capacity (Table S1). The $\text{FeSe}_2\text{-Fe}_2\text{O}_3$ and MB electrodes exhibited lower specific capacities than the $\text{FeSe}_x@C/MB$ and FeSe_x/MB electrodes, at all current densities. Also, to further confirm the advantages of 3D structured MXene for K^+ storage performance, bare 2D MXene was galvanostatically tested as anodes for KIBs under the same condition as the other electrode. As shown in Fig. S14a, b, the 2D MXene electrode exhibited lower reversible capacity over the entire cycle compared the MB electrode. In particular, the initial discharge capacity (163 mA h g^{-1}) of 2D MXene electrode was less than half that of the MB electrode (376 mA h g^{-1}). Furthermore, the difference in capacity between the two electrodes remained similar at various current densities from 0.1 to 3.0 A g^{-1} (Fig. S14c). These results indicate that the electrochemical performance of 3D MB electrode is better than that of the 2D MXene electrode, which can be attributed to a larger surface area and enhanced ion transport of 3D MB.

To elucidate the superior rate performance of $\text{FeSe}_x@C/MB$, CV measurements were carried out at scan rates in the $0.1\text{--}2.0 \text{ mV s}^{-1}$ range (Fig. 9). As shown in Fig. 9a, b, the redox peaks in the CV curves of $\text{FeSe}_x@C/MB$ and FeSe_x/MB gradually shifted with increasing the scan rate, owing to the electrode polarization [53]. The current density values of the apparent redox peaks in the CV curves of the two electrodes (denoted as peaks I and II, respectively) were fitted to logarithmic functions of the scan rate, according to the relationship $i = av^b$ (where i is the measured current, v is the scan rate, and both a and b are experimentally determined parameters) [63]. For b close to 1.0 , the electrochemical reaction is dominantly controlled by the capacitive behavior [64]. The b -values of $0.94, 0.95,$ and 0.99 respectively, for peaks I, II, and III of $\text{FeSe}_x@C/MB$ were higher than those of FeSe_x/MB , as shown in Fig. 9c, d, implying that $\text{FeSe}_x@C/MB$ has a more dominant capacitive property. Furthermore, the capacitive contribution values of $\text{FeSe}_x@C/MB$ and FeSe_x/MB , calculated based on the previously reported equation

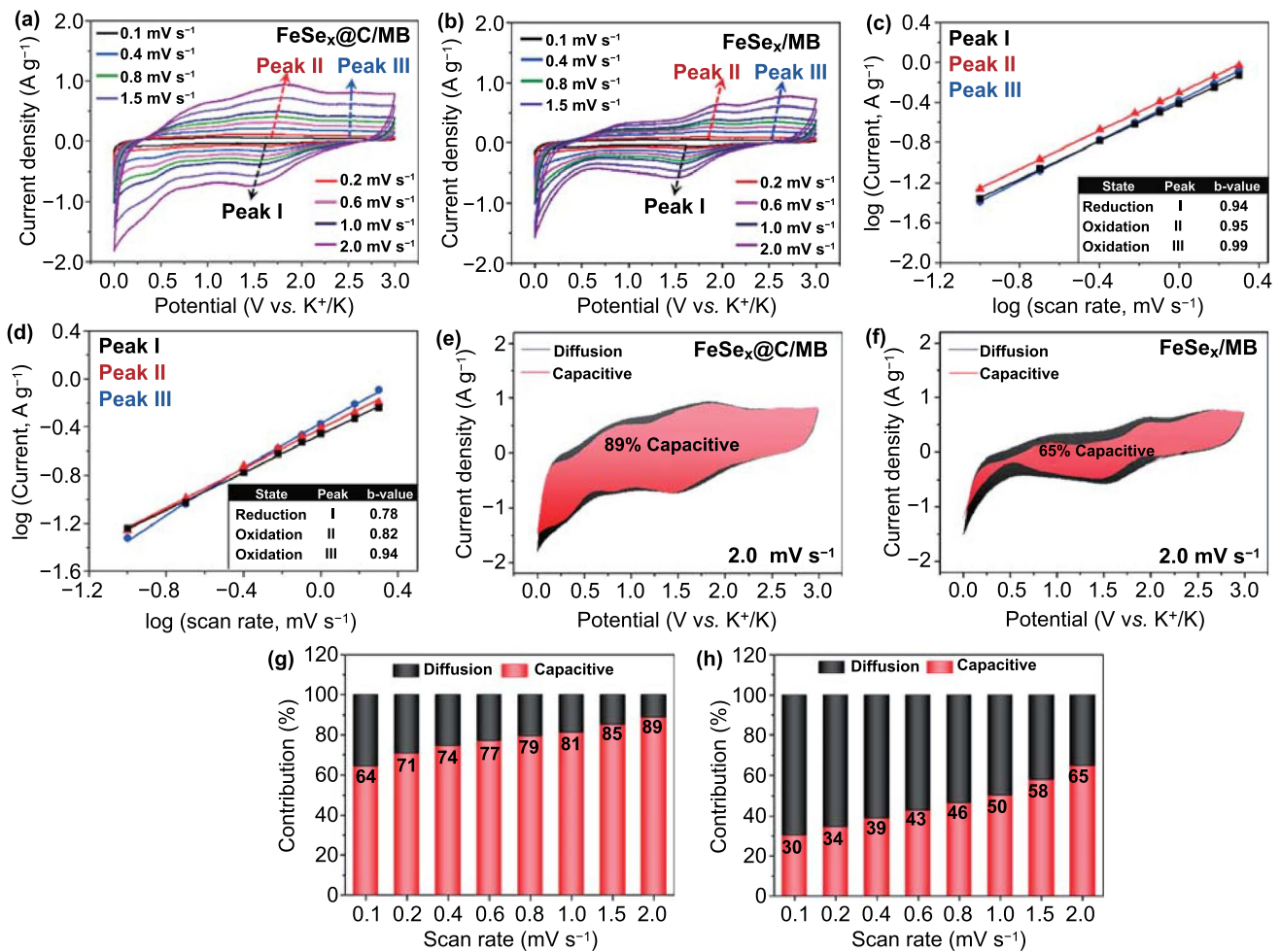


Fig. 9 a, b Cyclic voltammograms at various sweep rates, c, d fitted log (peak current) vs. log (scan rate) for peaks corresponding to certain electrochemical reactions, e, f cyclic voltammograms showing capacitive contribution (colored area) at a scan rate of 2.0 mV s⁻¹, and g, h capacity contribution at various scan rates of FeSe_x@C/MB and FeSe_x/MB

[65], gradually increased as the scan rate increased, reaching 89% and 65%, respectively, for the scan rate of 2.0 mV s⁻¹ (Fig. 9e–h). These high capacitive contributions represent the rapid electron transfer of FeSe_x@C/MB and support the rationale for its outstanding rate performance.

Ex-situ EIS measurements were performed to understand the charge transfer kinetics of the electrodes (Fig. 10). In the fresh state (Fig. 10a), the FeSe_x@C/MB electrode exhibited lower R_{ct} than the FeSe_x/MB electrode, indicating better charge transfer kinetics of the FeSe_x@C/MB electrode. After the first cycle, the R_{ct} values of the both electrodes decreased, which could be owing to the formation of ultrafine FeSe_x nanocrystals and electrode activation (Fig. 10b, c). Notably, the R_{ct} values of the FeSe_x@C/MB electrode changed

slightly as the cycling progressed, while those of FeSe_x/MB increased significantly after 160 cycles. These results arise from the increase in resistance owing to the pulverization of FeSe_x nanoparticles without the carbon coating in the FeSe_x/MB electrode during cycling. These results were in a good agreement with the cycle data (Fig. 8b). The linear slope in the low-frequency region of the Nyquist plot is associated with the Warburg impedance of potassium-ions' diffusion [66]. The relationship between the square root of the angular frequency ($\omega^{-1/2}$) and the real part impedance (Z') of the two electrodes cycled at the 160th cycle is presented in Fig. 10d. Compared with the result for the FeSe_x/MB electrode, the lower slope for the FeSe_x@C/MB electrode implies a faster diffusion of K⁺ ions after 160 cycles.

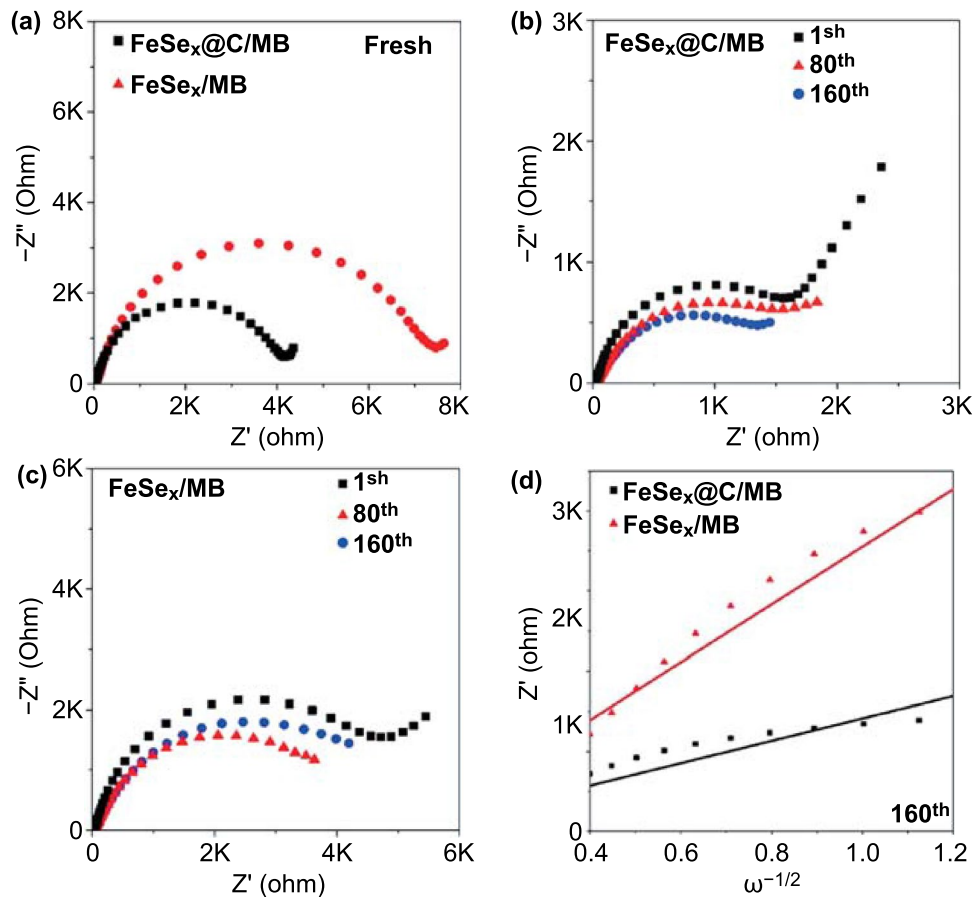


Fig. 10 Nyquist plots of of $\text{FeSe}_x\text{/C/MB}$ and $\text{FeSe}_x\text{/MB}$: **a** fresh cells, **b, c** after the 1st, 80th, and 160th cycle, and **d** the relationship between the phase angle ($\omega^{-1/2}$) and impedance (Z') at the 160th cycle

4 Conclusions

In summary, we report a novel strategy for designing carbon-coated 3D MXene/iron selenide balls with aggregation-resistant properties, for achieving high-performance KIBs. Using the ultrasonic spray pyrolysis method, 2D MXene nanosheets were easily converted into a corresponding 3D ball by rapid evaporation of droplets. The 3D MXene architectures featured a larger surface area, higher mechanical strength, and better accessibility for electrolytes and ions, while maintaining the attractive properties of MXene. Furthermore, combining iron selenides and carbon with 3D MXene balls offered many more sites for ion storage and enhanced the structural robustness of composite balls. Accordingly, the $\text{FeSe}_x\text{/C/MB}$ anode exhibited a high reversible capacity, long cycling stability, and an excellent rate capability, when used in KIBs. We believe that our strategy of synthesizing 3D MXene-based composites can also

be using for preparing other electrode materials for utilization in high-performance energy storage applications.

Acknowledgements This research was supported by the National Research Foundation of Korea (NRF) grant funded by Korea government (NRF-2019R1A2C2088047 and NRF-2020R1C1C1003375).

Funding Open access funding provided by Shanghai Jiao Tong University.

Open Access This article is licensed under a Creative Commons Attribution 4.0 International License, which permits use, sharing, adaptation, distribution and reproduction in any medium or format, as long as you give appropriate credit to the original author(s) and the source, provide a link to the Creative Commons licence, and indicate if changes were made. The images or other third party material in this article are included in the article's Creative Commons licence, unless indicated otherwise in a credit line to the material. If material is not included in the article's Creative Commons licence and your intended use is not permitted by statutory regulation or exceeds the permitted use, you will need to obtain

permission directly from the copyright holder. To view a copy of this licence, visit <http://creativecommons.org/licenses/by/4.0/>.

Supplementary Information The online version contains supplementary material available at <https://doi.org/10.1007/s40820-021-00741-0>.

References

- X.D. He, Z.H. Liu, J.Y. Liao, X. Ding, Q. Hu et al., A three-dimensional macroporous antimony@carbon composite as a high-performance anode material for potassium-ion batteries. *J. Mater. Chem. A* **7**(16), 9629–9637 (2019). <https://doi.org/10.1039/C9TA01968E>
- Y. Wu, Y. Sun, J. Zheng, J. Rong, H. Li et al., MXenes: advanced materials in potassium ion batteries. *Chem. Eng. J.* **404**, 126565 (2021). <https://doi.org/10.1016/j.cej.2020.126565>
- Z. Liu, H. Su, Y. Yang, T. Wu, S. Sun et al., Advances and perspectives on transitional metal layered oxides for potassium-ion battery. *Energy Stor. Mater.* **34**, 211–228 (2020). <https://doi.org/10.1016/j.ensm.2020.09.010>
- J. Jiang, G. Nie, P. Nie, Z. Li, Z. Pan et al., Nanohollow carbon for rechargeable batteries: ongoing progresses and challenges. *Nano-Micro Lett.* **12**, 183 (2020). <https://doi.org/10.1007/s40820-020-00521-2>
- B. Sheng, L. Wang, H. Huang, H. Yang, R. Xu et al., Boosting potassium storage by integration advantageous of defect engineering and spatial confinement: a case study of Sb_2Se_3 . *Small* **16**(49), 2005272 (2020). <https://doi.org/10.1002/sml.202005272>
- K. Xie, K. Yuan, X. Li, W. Lu, C. Shen et al., Superior potassium ion storage via vertical MoS_2 “nano-rose” with expanded interlayers on graphene. *Small* **13**(42), 1701471 (2017). <https://doi.org/10.1002/sml.201701471>
- Y. Zhao, J. Zhu, S.J.H. Ong, Q. Yao, X. Shi et al., High-rate and ultralong cycle-life potassium ion batteries enabled by in situ engineering of yolk–shell FeS_2 @C structure on graphene matrix. *Adv. Energy Mater.* **8**(36), 1802565 (2018). <https://doi.org/10.1002/aenm.201802565>
- X. Wu, H. Wang, Z. Zhao, B. Huang, Interstratification-assembled 2D black phosphorene and V_2CT_x MXene as superior anodes for boosting potassium-ion storage. *J. Mater. Chem. A* **8**(25), 12705–12715 (2020). <https://doi.org/10.1039/D0TA04506C>
- L. Bai, Y. Zhang, W. Tong, L. Sun, H. Huang et al., Graphene for energy storage and conversion: synthesis and interdisciplinary applications. *Electrochem. Energy Rev.* **3**(2), 395–430 (2020). <https://doi.org/10.1007/s41918-019-00042-6>
- J. Zheng, Y. Wu, Y. Sun, J. Rong, H. Li et al., Advanced anode materials of potassium ion batteries: from zero dimension to three dimensions. *Nano-Micro Lett.* **13**(1), 12 (2021). <https://doi.org/10.1007/s40820-020-00541-y>
- P. Huang, S. Zhang, H. Ying, Z. Zhang, W. Han, Few-layered Ti_3C_2 MXene anchoring bimetallic selenide NiCo_2Se_4 nanoparticles for superior sodium-ion batteries. *Chem. Eng. J.* **417**, 129161 (2021). <https://doi.org/10.1016/j.cej.2021.129161>
- Y. Dong, H. Shi, Z.S. Wu, Recent advances and promise of MXene-based nanostructures for high-performance metal ion batteries. *Adv. Funct. Mater.* **30**(47), 2000706 (2020). <https://doi.org/10.1002/adfm.202000706>
- F. Ming, H. Liang, G. Huang, Z. Bayhan, H.N. Alshareef, MXenes for rechargeable batteries beyond the lithium-ion. *Adv. Mater.* **33**(1), 2004039 (2021). <https://doi.org/10.1002/adma.202004039>
- Y.J. Lei, Z.C. Yan, W.H. Lai, S.L. Chou, Y.X. Wang et al., Tailoring MXene-based materials for sodium-ion storage: synthesis, mechanisms, and applications. *Electrochem. Energy Rev.* **3**, 766–792 (2020). <https://doi.org/10.1007/s41918-020-00079-y>
- R. Zhao, H. Di, X. Hui, D. Zhao, R. Wang et al., Self-assembled Ti_3C_2 MXene and N-rich porous carbon hybrids as superior anodes for high-performance potassium-ion batteries. *Energy Environ. Sci.* **13**(1), 246–257 (2020). <https://doi.org/10.1039/C9EE03250A>
- P. Lian, Y. Dong, Z.S. Wu, S. Zheng, X. Wang et al., Alkalized Ti_3C_2 MXene nanoribbons with expanded interlayer spacing for high-capacity sodium and potassium ion batteries. *Nano Energy* **40**, 1–8 (2017). <https://doi.org/10.1016/j.nanoen.2017.08.002>
- M.Q. Zhao, X. Xie, C.E. Ren, T. Makaryan, B. Anasori et al., Hollow MXene spheres and 3D macroporous MXene frameworks for Na-ion storage. *Adv. Mater.* **29**(37), 1702410 (2017). <https://doi.org/10.1002/adma.201702410>
- G. Tontini, M. Greaves, S. Ghosh, V. Bayram, S. Barg, MXene-based 3D porous macrostructures for electrochemical energy storage. *J. Phys. Mater.* **3**, 022001 (2020). <https://doi.org/10.1088/2515-7639/ab78f1>
- P. Zhang, R.A. Soomro, Z. Guan, N. Sun, B. Xu, 3D carbon-coated MXene architectures with high and ultrafast lithium/sodium-ion storage. *Energy Stor. Mater.* **29**, 163–171 (2020). <https://doi.org/10.1016/j.ensm.2020.04.016>
- J. Li, L. Han, Y. Li, J. Li, G. Zhu et al., MXene-decorated $\text{SnS}_2/\text{Sn}_3\text{S}_4$ hybrid as anode material for high-rate lithium-ion batteries. *Chem. Eng. J.* **380**, 122590 (2020). <https://doi.org/10.1016/j.cej.2019.122590>
- E. Xu, Y. Zhang, H. Wang, Z. Zhu, J. Quan et al., Ultrafast kinetics net electrode assembled via $\text{MoSe}_2/\text{MXene}$ heterojunction for high-performance sodium-ion batteries. *Chem. Eng. J.* **385**, 123839 (2020). <https://doi.org/10.1016/j.cej.2019.123839>
- Z. Xia, X. Chen, H. Ci, Z. Fan, Y. Yi et al., Designing N-doped graphene/ $\text{ReSe}_2/\text{Ti}_3\text{C}_2$ MXene heterostructure frameworks as promising anodes for high-rate potassium-ion batteries. *J. Energy Chem.* **53**, 155–162 (2021). <https://doi.org/10.1016/j.jechem.2020.04.071>
- J. Cao, L. Wang, D. Li, Z. Yuan, H. Xu et al., $\text{Ti}_3\text{C}_2\text{T}_x$ MXene conductive layers supported bio-derived $\text{Fe}_{x-1}\text{Se}_x/\text{MXene}/$ carbonaceous nanoribbons for high-performance half/full sodium-ion and potassium-ion batteries. *Adv. Mater.* **33**(34), 2101535 (2021). <https://doi.org/10.1002/adma.202101535>



24. G.D. Park, Y.C. Kang, One-pot synthesis of CoSe_x -rGo composite powders by spray pyrolysis and their application as anode material for sodium-ion batteries. *Chem. Eur. J.* **22**(12), 4140–4146 (2016). <https://doi.org/10.1002/chem.201504398>
25. Y.N. Ko, S.H. Choi, Y.C. Kang, Hollow cobalt selenide microspheres: synthesis and application as anode materials for Na-ion batteries. *ACS Appl. Mater. Interfaces* **8**(10), 6449–6456 (2016). <https://doi.org/10.1021/acsami.5b11963>
26. G.D. Park, J.K. Lee, Y.C. Kang, Synthesis of uniquely structured SnO_2 hollow nanoplates and their electrochemical properties for Li-ion storage. *Adv. Funct. Mater.* **27**(4), 1603399 (2017). <https://doi.org/10.1002/adfm.201603399>
27. M. Alhabeab, K. Maleski, B. Anasori, P. Lelyukh, L. Clark et al., Guidelines for synthesis and processing of two-dimensional titanium carbide ($\text{Ti}_3\text{C}_2\text{T}_x$ MXene). *Chem. Mater.* **29**(18), 7633–7644 (2017). <https://doi.org/10.1021/acs.chemmater.7b02847>
28. F. Zhang, Y. Zhou, Y. Zhang, D. Li, Z. Huang, Facile synthesis of sulfur@titanium carbide MXene as high performance cathode for lithium-sulfur batteries. *Nanophotonics* **9**(7), 2025–2032 (2020). <https://doi.org/10.1515/nanoph-2019-0568>
29. M. Han, X. Yin, H. Wu, Z. Hou, C. Song et al., Ti_3C_2 MXenes with modified surface for high-performance electromagnetic absorption and shielding in the X-band. *ACS Appl. Mater. Interfaces* **8**(32), 21011–21019 (2016). <https://doi.org/10.1021/acsami.6b06455>
30. Y. Chen, J. Shao, X. Lin, Y. Gu, R. Holze et al., Hollow structured carbon@FeSe nanocomposite as a promising anode material for Li-ion batteries. *ChemElectroChem* **6**(5), 1393–1399 (2019). <https://doi.org/10.1002/celec.201801722>
31. D. Li, J. Zhou, X. Chen, H. Song, Achieving ultrafast and stable Na-ion storage in FeSe_2 nanorods/graphene anodes by controlling the surface oxide. *ACS Appl. Mater. Interfaces* **10**(26), 22841–22850 (2018). <https://doi.org/10.1021/acsami.8b06318>
32. B. He, G. Li, J. Li, J. Wang, H. Tong et al., MoSe_2 @CNT core-shell nanostructures as grain promoters featuring a direct Li_2O_2 formation/decomposition catalytic capability in lithium-oxygen batteries. *Adv. Energy Mater.* **11**(18), 2003263 (2021). <https://doi.org/10.1002/aenm.202003263>
33. R. Xu, Y. Yao, H. Wang, Y. Yuan, J. Wang et al., Unraveling the nature of excellent potassium storage in small-molecule Se@peapod-like N-doped carbon nanofibers. *Adv. Mater.* **32**(52), 2003879 (2020). <https://doi.org/10.1002/adma.202003879>
34. J. Halim, K.M. Cook, M. Naguib, P. Eklund, Y. Gogotsi et al., X-ray photoelectron spectroscopy of select multi-layered transition metal carbides (MXenes). *Appl. Surf. Sci.* **362**, 406–417 (2016). <https://doi.org/10.1016/j.apsusc.2015.11.089>
35. C. Shen, L. Wang, A. Zhou, B. Wang, X. Wang et al., Synthesis and electrochemical properties of two-dimensional rGo/ $\text{Ti}_3\text{C}_2\text{T}_x$ nanocomposites. *Nanomaterials* **8**(2), 80 (2018). <https://doi.org/10.3390/nano8020080>
36. E. Satheshkumar, T. Makaryan, A. Melikyan, H. Minassian, Y. Gogotsi et al., One-step solution processing of Ag, Au and Pd@MXene hybrids for SERS. *Sci. Rep.* **6**(1), 32049 (2016). <https://doi.org/10.1038/srep32049>
37. V. Natu, M. Benchakar, C. Canaff, A. Habrioux, S. Celerier et al., A critical analysis of the X-ray photoelectron spectra of $\text{Ti}_3\text{C}_2\text{T}_z$ MXenes. *Matter* **4**(4), 1224–1251 (2021). <https://doi.org/10.1016/j.matt.2021.01.015>
38. S.Y. Jeong, J.S. Cho, Porous hybrid nanofibers comprising $\text{ZnSe}/\text{CoSe}_2$ /carbon with uniformly distributed pores as anodes for high-performance sodium-ion batteries. *Nanomaterials* **9**(10), 1362 (2019). <https://doi.org/10.3390/nano9101362>
39. S. Ji, L. Zhang, L. Yu, X. Xu, J. Liu, In situ carbon-coating and Ostwald ripening-based route for hollow Ni_3S_4 @C spheres with superior Li-ion storage performances. *RSC Adv.* **6**(104), 101752–101759 (2016). <https://doi.org/10.1039/C6RA21677C>
40. B. Yuan, W. Luan, S. Tu, One-step synthesis of cubic FeS_2 and flower-like FeSe_2 particles by a solvothermal reduction process. *Dalton Trans.* **41**(3), 772–776 (2012). <https://doi.org/10.1039/C1DT11176K>
41. X. Wei, C. Tang, Q. An, M. Yan, X. Wang et al., FeSe_2 clusters with excellent cyclability and rate capability for sodium-ion batteries. *Nano Res.* **10**(9), 3202–3211 (2017). <https://doi.org/10.1007/s12274-017-1537-z>
42. W. Feng, H. Luo, Y. Wang, S. Zeng, Y. Tan et al., MXenes derived laminated and magnetic composites with excellent microwave absorbing performance. *Sci. Rep.* **9**(1), 3957 (2019). <https://doi.org/10.1038/s41598-019-40336-9>
43. K. Krishnamoorthy, P. Pazhamalai, S. Sahoo, S.J. Kim, Titanium carbide sheet based high performance wire type solid state supercapacitors. *J. Mater. Chem. A* **5**(12), 5726–5736 (2017). <https://doi.org/10.1039/C6TA11198J>
44. H. Kim, B. Anasori, Y. Gogotsi, H.N. Alshareef, Thermoelectric properties of two-dimensional molybdenum-based MXenes. *Chem. Mater.* **29**(15), 6472–6479 (2017). <https://doi.org/10.1021/acs.chemmater.7b02056>
45. Z. Li, L. Wang, D. Sun, Y. Zhang, B. Liu et al., Synthesis and thermal stability of two-dimensional carbide MXene Ti_3C_2 . *Mater. Sci. Eng. B* **191**, 33–40 (2015). <https://doi.org/10.1016/j.mseb.2014.10.009>
46. J.S. Park, S.Y. Jeong, K.M. Jeon, Y.C. Kang, J.S. Cho, Iron diselenide combined with hollow graphitic carbon nanospheres as a high-performance anode material for sodium-ion batteries. *Chem. Eng. J.* **339**, 97–107 (2018). <https://doi.org/10.1016/j.cej.2018.01.118>
47. S. Kajiyama, L. Szabova, K. Sodeyama, H. Iinuma, R. Morita et al., Sodium-ion intercalation mechanism in MXene nanosheets. *ACS Nano* **10**(3), 3334–3341 (2016). <https://doi.org/10.1021/acs.nano.5b06958>
48. Y. Yi, Z. Sun, C. Li, Z. Tian, C. Lu et al., Designing 3D biomorphic nitrogen-doped MoSe_2 /graphene composites toward high-performance potassium-ion capacitors. *Adv. Funct. Mater.* **30**(4), 1903878 (2020). <https://doi.org/10.1002/adfm.201903878>
49. B. Tian, W. Tang, C. Su, Y. Li, Reticular $\text{V}_2\text{O}_5 \cdot 0.6\text{H}_2\text{O}$ xerogel as cathode for rechargeable potassium ion batteries. *ACS Appl. Mater. Interfaces* **10**(1), 642–650 (2018). <https://doi.org/10.1021/acsami.7b15407>
50. S.H. Lim, G.D. Park, D.S. Jung, J.H. Lee, Y.C. Kang, Towards an efficient anode material for Li-ion batteries: understanding

- the conversion mechanism of nickel hydroxy chloride with Li-ions. *J. Mater. Chem. A* **8**(4), 1939–1946 (2020). <https://doi.org/10.1039/C9TA12321K>
51. J. Liu, S. Xiao, X. Li, Z. Li, X. Li et al., Interface engineering of Fe₃Se₄/FeSe heterostructure encapsulated in electrospun carbon nanofibers for fast and robust sodium storage. *Chem. Eng. J.* **417**, 129279 (2021). <https://doi.org/10.1016/j.cej.2021.129279>
52. Y. Tang, Z. Zhao, X. Hao, Y. Wei, H. Zhang et al., Cellular carbon-wrapped FeSe₂ nanocavities with ultrathin walls and multiple rooms for ion diffusion-confined ultrafast sodium storage. *J. Mater. Chem. A* **7**(9), 4469–4479 (2019). <https://doi.org/10.1039/C8TA10614B>
53. J.K. Kim, Y.C. Kang, Encapsulation of Se into hierarchically porous carbon microspheres with optimized pore structure for advanced Na–Se and K–Se batteries. *ACS Nano* **14**(10), 13203–13216 (2020). <https://doi.org/10.1021/acsnano.0c04870>
54. Y. Liu, C. Yang, Y. Li, F. Zheng, Y. Li et al., FeSe₂/nitrogen-doped carbon as anode material for potassium-ion batteries. *Chem. Eng. J.* **393**, 124590 (2020). <https://doi.org/10.1016/j.cej.2020.124590>
55. H. Min, M. Li, H. Shu, X. Zhang, T. Hu et al., FeSe₂ nanoparticle embedded in 3D honeycomb-like N-doped carbon architectures coupled with electrolytes engineering boost superior potassium ion storage. *Electrochim. Acta* **366**, 137381 (2021). <https://doi.org/10.1016/j.electacta.2020.137381>
56. Z. Wang, X. Zhang, Y. Zhao, M. Li, T. Tan et al., Preparation and electrochemical properties of pomegranate-shaped Fe₂O₃/C anodes for Li-ion batteries. *Nanoscale Res. Lett.* **13**(1), 344 (2018). <https://doi.org/10.1186/s11671-018-2757-1>
57. L. Ji, O. Toprakci, M. Alcoutlabi, Y. Yao, Y. Li et al., α -Fe₂O₃ nanoparticle-loaded carbon nanofibers as stable and high-capacity anodes for rechargeable lithium-ion batteries. *ACS Appl. Mater. Interfaces* **4**(5), 2672–2679 (2012). <https://doi.org/10.1021/am300333s>
58. B. Ahmed, D.H. Anjum, Y. Gogotsi, H.N. Alshareef, Atomic layer deposition of SnO₂ on MXene for Li-ion battery anodes. *Nano Energy* **34**, 249–256 (2017). <https://doi.org/10.1016/j.nanoen.2017.02.043>
59. Z. Lin, H. Shao, K. Xu, P.L. Taberna, P. Simon, MXenes as high-rate electrodes for energy storage. *Trends Chem.* **2**(7), 654–664 (2020). <https://doi.org/10.1016/j.trechm.2020.04.010>
60. X. Li, M. Zhang, S. Yuan, C. Lu, Research progress of silicon/carbon anode materials for lithium-ion batteries: Structure design and synthesis method. *ChemElectroChem* **7**(21), 4289–4302 (2020). <https://doi.org/10.1002/celec.202001060>
61. M.M. Gaikwad, C.S. Sharma, In situ graphitized hard carbon xerogel: a promising high-performance anode material for Li-ion batteries. *J. Mater. Res.* **35**(21), 2989–3003 (2020). <https://doi.org/10.1557/jmr.2020.293>
62. D.Y. Jo, J.K. Kim, H.G. Oh, Y.C. Kang, S.K. Park, Chemically integrating MXene nanosheets with N-doped C-coated Si nanoparticles for enhanced Li storage performance. *Scr. Mater.* **199**, 113840 (2021). <https://doi.org/10.1016/j.scripamat.2021.113840>
63. Y. Fang, X.Y. Yu, X.W. Lou, Formation of hierarchical Cu-doped CoSe₂ microboxes via sequential ion exchange for high-performance sodium-ion batteries. *Adv. Mater.* **30**(21), 1706668 (2018). <https://doi.org/10.1002/adma.201706668>
64. F. Jiang, Y. Bai, L. Zhang, W. Zhao, P. Ge et al., Modified bornite materials with high electrochemical performance for sodium and lithium storage. *Energy Stor. Mater.* **40**, 150–158 (2021). <https://doi.org/10.1016/j.ensm.2021.04.046>
65. R. Sun, S. Liu, Q. Wei, J. Sheng, S. Zhu et al., Mesoporous NiS₂ nanospheres anode with pseudocapacitance for high-rate and long-life sodium-ion battery. *Small* **13**(39), 1701744 (2017). <https://doi.org/10.1002/sml.201701744>
66. Y. Che, X. Lin, L. Xing, X. Guan, R. Guo et al., Protective electrode/electrolyte interphases for high energy lithium-ion batteries with p-toluenesulfonyl fluoride electrolyte additive. *J. Energy Chem.* **52**, 361–371 (2021). <https://doi.org/10.1016/j.jechem.2020.04.023>

